

Magnetic penetration depth in the Chevrel-phase superconductors $\text{SnMo}_6\text{S}_{8-x}\text{Se}_x$ and $\text{PbMo}_6\text{S}_{8-x}\text{Se}_x$

P. Birrer,* F. N. Gygax, B. Hitti,[†] E. Lippelt, A. Schenck, and M. Weber
*Institute for Intermediate Energy Physics, Eidgenössische Technische Hochschule Zürich,
 CH-5232 Villigen PSI, Switzerland*

D. Cattani, J. Cors, M. Decroux, and Ø. Fischer
Departement de Physique de la Matière Condensée, Université de Genève, CH-1211 Genève 4, Switzerland
 (Received 20 May 1993)

A full account of positive-muon spin-rotation (μ^+ SR) studies on the systematics of the magnetic penetration depth λ in the isotropic Chevrel-phase superconductors $\text{SnMo}_6\text{S}_{8-x}\text{Se}_x$ ($x=0,1,4,7$) and $\text{PbMo}_6\text{S}_{8-x}\text{Se}_x$ ($x=0,4$) is presented. The absolute determination of λ from the μ SR data necessitates a careful analysis of the μ SR line shape and a comparison with simulated data, taking into account distortions of the flux-line lattice and a distribution of demagnetization factors in the sintered granular polycrystalline probes investigated. A correlation between T_c and $1/\lambda^2$ is found which supports a recently developed quantum percolation model.

I. INTRODUCTION

The ternary molybdenum chalcogenide—so-called Chevrel-phase—superconductors display, like the high-temperature oxide superconductors, an extreme type-II superconductivity. The Ginsburg-Landau parameter κ is large (≈ 100) and the coherence length ξ may be extremely short, i.e., of the order of the lattice parameters. Correspondingly huge upper critical fields H_{c2} are observed and in fact, before the discovery of the high-temperature oxide superconductors, a record value of $H_{c2} = 60$ T was observed in PbMo_6S_8 .¹

Recent studies in high-temperature superconductors have suggested a kind of universal relationship between the transition temperature T_c and the superconducting charge-carrier density n_s ,²⁻⁵ which has been interpreted in terms of a model in which superconductivity is a result of local pair formation or Bose-Einstein condensation like in superfluid ^4He .⁶⁻⁹ It seems that this picture can be extended to other systems showing an extreme type-II superconductivity, namely the bismuthates, organic superconductors, heavy-fermion compounds, the fullerenes, and the Chevrel-phase superconductors.^{6,10} In this contribution we will present a comprehensive analysis of results obtained by positive-muon spin-rotation (μ^+ SR) spectroscopy in solid solutions of Chevrel-phase compounds of the composition $\text{SnMo}_6\text{S}_{8-x}\text{Se}_x$ and $\text{PbMo}_6\text{S}_{8-x}\text{Se}_x$.

The ternary molybdenum chalcogenides crystallize in a hexagonal-rhombohedral structure. The composition $M\text{Mo}_6X_8$ is obtained for cations M with a large ionic radius (Pb, Sn, La, rare earth).¹ The basic building blocks are the “molecules” Mo_6X_8 which interact only weakly with each other. The conduction-electron band derives from the Mo $4d$ electrons and is rather narrow due to the weak overlap of the Mo_6X_8 molecular d -electron states.¹ Therefore, the superconductivity of Chevrel-phase com-

pounds is primarily a property of the Mo_6X_8 clusters. (Note that the binary Chevrel-phase compound Mo_6Se_8 also displays superconductivity.) The superconducting transition temperature T_c differs widely from compound to compound. It is this property which makes the Chevrel-phase compounds an interesting object for study, since it allows one to study the correlation of T_c with other properties of these compounds. The variation of T_c seems to be primarily determined by electronic properties and does not seem to arise from different phonon spectra. The effect of the type of cation on T_c is thought to arise from two different sources: (1) the amount of charge transfer from the cation to the Mo_6X_8 cluster determines sensitively the position of the Fermi level and hence the Fermi level density of states; (2) the type of cation modifies the distance between the Mo_6X_8 clusters and therefore the width and position of the narrow conduction band, affecting again the Fermi level density of states. Indeed it is found that T_c shows a pronounced correlation with the volume of the hexagonal unit cell¹¹ as well as with the valence electron concentration on the Mo_6X_8 cluster.¹² It should be mentioned that the shortest intracluster Mo-Mo distance is rather insensitive to the type of cation M and the chalcogen X .¹ T_c changes also with the type of chalcogen. For $X = \text{Te}$ no superconductivity is observed (an exception is $\text{Mo}_4\text{Re}_2\text{Te}_8$). In solid solutions of the type $M\text{Mo}_6\text{S}_{8-x}\text{Se}_x$, T_c is observed to change smoothly with x , displaying a minimum for $x \approx 0.4$.¹³ It has been suggested that in the solid solutions the threefold rotational symmetry around the hexagonal c axis is destroyed, which lifts the degeneracy of certain cluster d -electron states and results in a general reduction of the density of states.¹⁴ In the case of $X = \text{Se}, \text{Te}$ the charge state of these ions seems to be less than -2 (i.e., more positive), leading therefore to an increased number of conduction d electrons per Mo_6X_8 cluster and shifting the Fermi level to a higher value.

In trying to elucidate the functional dependence of T_c on the density of charge carriers (and in order to understand the mechanism behind this functional dependence), one encounters the problem of knowing the carrier concentration in some reliable way. Hall-effect measurements could, in principle, serve this purpose, but are plagued by several problems related to the probable presence of both hole and electron charge carriers.¹⁵ The sign of the Hall coefficient is generally found to be positive, indicating a dominating influence of hole carriers, e.g., because they possess a larger mobility than the electron carriers. Without knowing more about the mobilities it is not possible to extract the carrier densities unambiguously. In addition the mobilities are expected to be critically affected by impurities and/or vacancies and therefore strong sample-dependent features could be involved if an excellent control over the sample quality is not achieved.

A more reliable way of determining the charge-carrier concentration, which we apply in this study, is to measure the magnetic penetration depth λ , which in the clean limit is related to the superconducting charge-carrier density n_s by the expression¹⁶

$$\lambda_L = \left[\frac{m^* c^2}{4\pi e^2 n_s} \right]^{1/2} = \left[\frac{m^*/m_0}{4\pi r_c n_s} \right]^{1/2}. \quad (1)$$

Here m^* is the effective charge-carrier mass and r_c is the classical electron radius. For not so perfect superconductors with a reduced mean free-electron path l one has to use instead¹⁶

$$\lambda = \left[\frac{m^*/m}{4\pi r_c n_s} (1 + \xi_0/l) \right]^{1/2}, \quad (2)$$

where ξ_0 is the intrinsic coherence length. The problem then is to know the quantity l . As will be discussed in Sec. V this quantity is usually not very well determined. But since ξ_0 is rather small, as pointed out above, the error in the determination of n_s may never be larger than ~40% (i.e., we assume $\xi/l < 1$).

In this work the penetration depth λ is determined from μ SR-spectroscopy measurements.¹⁷ Some principal considerations on the applicability of this method are presented in the next section. The paper is further organized as follows. Section III provides experimental details, including the sample preparation; in Sec. IV the results are presented and the extraction of λ from the μ SR data is described, the systematics of λ and some further consequences are discussed in Sec. V, followed in Sec. VI by a summary.

This work supersedes a previous preliminary report by Birrer *et al.*¹⁸

II. ON THE DETERMINATION OF λ FROM μ SR SPECTRA

The internal field distribution $\mathbf{h}(\mathbf{r})$ in the mixed state of an isotropic superconductor can be calculated with the help of the London equation.¹⁶ $h(\mathbf{r})$ is governed by just the penetration depth λ .

Spin-polarized positive muons (μ^+) implanted randomly into a Type-II superconductor in the mixed state

with their spins perpendicular to the average magnetic flux $\mathbf{B}_0 = \langle \mathbf{h}(\mathbf{r}) \rangle$ will start to precess with frequencies $\omega(\mathbf{r}) = \gamma_\mu h(\mathbf{r})$. The spectral distribution of the precession frequencies $F(\omega)$ follows from the expression

$$F(\omega) = \gamma_\mu \frac{1}{S} \int \int \delta(h - h(\mathbf{r})) d^2r, \quad (3)$$

where $\delta(h - h(\mathbf{r}))$ denotes the Dirac δ function and S is the area of the two-dimensional unit cell of the flux lattice. If the evolution of the polarization $\mathbf{P}(t)$ of the implanted μ^+ ensemble is monitored along the initial polarization $\mathbf{P}(0) = \mathbf{P}_x(0) = P(0) \cdot \mathbf{x}_0$ [$\mathbf{P}(0)$ defines the x axis, \mathbf{x}_0 is a unit vector, \mathbf{B} defines the z axis], $P_x(t)$ is given by the Fourier transform

$$\begin{aligned} P_x(t) &= \mathbf{P}(t) \cdot \mathbf{x}_0 \\ &= \text{Re} \left\{ \frac{1}{2\pi} \int_0^\infty F(\omega) e^{i\omega t} d\omega \right\} \\ &= \text{Re} \left\{ \frac{1}{2\pi} \int_0^\infty F(\omega) e^{i(\omega - \omega_0)t} d\omega \right\} \cos \omega_0 t \\ &= G(t) \cos \omega_0 t. \end{aligned} \quad (4)$$

Here ω_0 is the average frequency following from

$$\omega_0 = \int_0^\infty \omega F(\omega) d\omega = \gamma_\mu B_0 \quad (5)$$

and $G(t)$ is a relaxation function which, due to the complicated form of $F(\omega)$, has no analytical solution. Nevertheless very often μ SR spectra are analyzed by assuming $G(t)$ to be given by

$$G(t) = \exp(-\frac{1}{2}\sigma^2 t^2), \quad (6)$$

where σ^2 is identified with the second moment of the distribution $F(\omega)$, i.e.,¹⁹

$$\sigma^2 = 0.0037 \gamma_\mu^2 \phi_0^2 / \lambda^4 \quad (7)$$

for $\lambda >$ flux lattice constant ($\phi_0 =$ flux quantum). This procedure, however, can lead to quite an erroneous determination of λ , since the Gaussian approximation [Eq. (6)] is often too crude. This can be seen from Fig. 1. It shows a plot of λ versus σ_G where σ_G is obtained by fitting Eq. (6) to simulated data (curve labeled 0.00). For more details on the data simulation see Ref. 20 and Sec. IV. By comparison the dashed curve represents just Eq. (7). The difference is obvious.

Besides the field distribution arising from the flux-line lattice (assumed to be absolutely regular so far) there may be other contributions that have to be folded in: (i) nuclear dipole fields; the spectral distribution of these is Gaussian and the width is given by the Van Vleck second-moment formula or modifications of it.¹⁷ This width, in frequency units, is denoted by σ_n . (ii) random small displacements of the vortices out of their rigid-lattice positions, due to the unavoidable presence of pinning centers (defects, lattice irregularities, etc.); the flux-line lattice created in a field-cooling procedure will never be perfect. According to Brandt²¹ this can be approximately accounted for by convoluting $F(\omega)$ with a Gaussian distribution of width $\bar{\sigma}_a$. An average displacement of

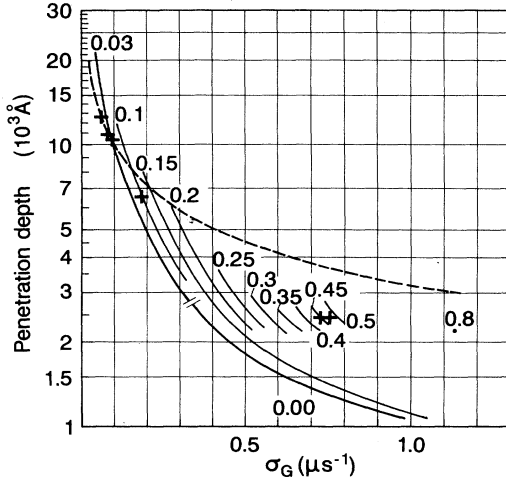


FIG. 1. Correlation between the magnetic penetration depth λ and the Gaussian relaxation rate σ_G obtained by fitting Eq. (6) to simulated μ SR spectra. The value (in μs^{-1}) attached to each curve denotes the width of an additional Gaussian field distribution with which the field distribution arising from the vortex lattice is convoluted. The dashed curve represents Eq. (7). The crosses denote results from our measurements.

3% will lead to a width of $\bar{\sigma}_a \approx \gamma_\mu 0.2M$, where M is the magnetization of the sample in the mixed state.²¹ (iii) In the case of granular polycrystalline samples (as in our case) a distribution in demagnetization factors may be expected which manifests itself via the average field inside a grain:²²

$$B_0 = B_{\text{ext}} - N_s \mathbf{M}_s + N_h \mathbf{M}_s + (4\pi - N_g) \mathbf{M}_m . \quad (8)$$

Here M_m is the negative (Meissner) magnetization of a single grain due to the diamagnetism in the superconducting state after cooling in a nonzero external field B_{ext} through T_c (field cooling) and M_s is the total negative magnetization of the whole sample (per unit volume). M_m and M_s are related to each other via $M_s = \rho_g / \rho_s M_m$ (ρ_g is the crystalline density, ρ_s is the effective sample density). The various terms have the following meaning: $-N_s \mathbf{M}_s$ is the global demagnetization field arising from the whole sample, $N_h \mathbf{M}_s$ is the field associated with the hole that would emerge when the μ^+ containing grain is removed, $-N_g \mathbf{M}_m$ is the demagnetization field associated with this grain, $4\pi \mathbf{M}_m$ is the field inside this grain due to the diamagnetic response. N_s, N_h, N_g are the demagnetization factors of the whole sample, the holes and the individual grains, respectively. Since each grain has a different N_g (but M_m is supposed to be the same in all grains), an additional broadening of the overall field distribution is to be expected. For simplicity we assume that N_g is Gaussian distributed with a width of $\Delta N_g \cdot M_m$. Also N_h may vary, but perhaps less than N_g does. In any case we exclude $N_h = N_g$ in view of the noncompact packing of grains. On average we assume $\langle N_h \rangle = \langle N_g \rangle = 4\pi/3$, i.e., it is assumed that the granular structure has no effect on the overall average B_0 .

The three Gaussian distributions discussed above may be combined to form a single Gaussian distribution with a width (in frequency units) of

$$\sigma_s = [\sigma_n^2 + \bar{\sigma}_a^2 + (\gamma_\mu \Delta N_g M_m)^2]^{1/2} . \quad (9)$$

The overall spectral frequency distribution is then obtained by convoluting $F(\omega)$ with a Gaussian distribution of width σ_a . Assuming various values for σ_a simulated data have again been generated and analyzed as described below in Sec. IV. The resulting λ versus σ_G curves are shown in Fig. 1 as well. The labels represent σ_a in μs^{-1} . If some independent knowledge on σ_a is available this graph may help in determining the true λ from a Gaussian fit [Eq. (6)] of μ^+ relaxation data.

Given all these complications we prefer to analyze the data in a different way. Our approach, described in detail in Ref. 20, consists in the comparison of simulated and measured μ SR spectra, in particular Fourier transforms of original and simulated time spectra. This will be described in Sec. IV. Compared to the analysis of μ SR data obtained in granular polycrystalline high-temperature superconductors, the situation is much simpler in the present case because of the isotropic properties of the Chevrel-phase superconductors and the absence of problems related to the anisotropy of the penetration depth and the (field-cooled) magnetization.

III. EXPERIMENTAL DETAILS

A. Samples

All samples ($\text{SnMo}_6\text{S}_{8-x}\text{Se}_x$, $x=0,1,4,7$; $\text{PbMo}_6\text{S}_{8-x}\text{Se}_x$, $x=0,4$) were prepared in the Département de Physique de la Matière Condensée of the University of Geneva. In a first step the MoS_2 , Mo_2Se_3 , PbS , and SnS precursors are synthesized by a solid-state reaction of the appropriate amount of each element. The reaction is carried out in an evacuated quartz tube at 900°C for 48 h. In a second step the Chevrel phase is synthesized by reacting the needed quantity of each precursor. The reaction is carried out either in an evacuated quartz tube for 60 h at 1150°C or in a boron nitride crucible sealed by thermal compression and heated at 1600°C for 2 h. The latter process²³ yielded rather perfect crystalline materials as evidenced by the sharpness of the x-ray-diffraction patterns. Furthermore, this process avoids oxygen contamination inherently present when quartz tubes are used at temperatures exceeding 1000°C .

In a third step the powder is sintered in a furnace by pressing it for 90 min with 0.2 kbar at a temperature of 1230°C . The samples produced in this way possessed the form of flat discs with 14 mm diam and 2.3 mm thickness. The effective density corresponded to 70–80% of the maximum possible value. $\text{SnMo}_6\text{S}_4\text{Se}_4$ and $\text{PbMo}_6\text{S}_4\text{Se}_4$ were prepared by following in the second step the first approach and the other samples by following the second approach.

X-ray analysis was used to search for foreign phases in the final samples. Only the samples which showed no sign for the presence of foreign phases ($< 5\%$, limit of

sensitivity in the x-ray analysis) were used in the further study.

The transition temperature T_c into the superconducting phase was determined from low-field ac susceptibility (χ_{ac}) measurements. As an example Fig. 2 displays the results obtained in $\text{SnMo}_6\text{S}_{8-x}\text{Se}_x$ ($x=0,1,7$). The different shapes of $\chi_{ac}(T)$ are related to the grain sizes and the intergrain couplings.²⁴ The fast initial decrease of χ_{ac} below T_c seen in Fig. 2(a) is associated with intragrain currents, while the slower decrease at lower temperatures is associated with intergrain currents. In Table I we quote both the onset of superconductivity temperature $T_{c,0}$, determined by the first sign of a decrease of χ_{ac} , and the temperature $T_{c,10\%}$ at which $|\chi_{ac}|$ has reached 10% of its low-temperature saturation value. In addition Table I includes critical temperatures following from the μSR data (see Sec. IV). Average temperatures \bar{T}_c are listed in Table II.

Magnetization measurements with a superconducting quantum interference device (SQUID) magnetometer were performed on the SnMo_6S_8 sample.²⁵ From these measurements H_{c1} was determined to be $H_{c1} \cong 110$ Oe.

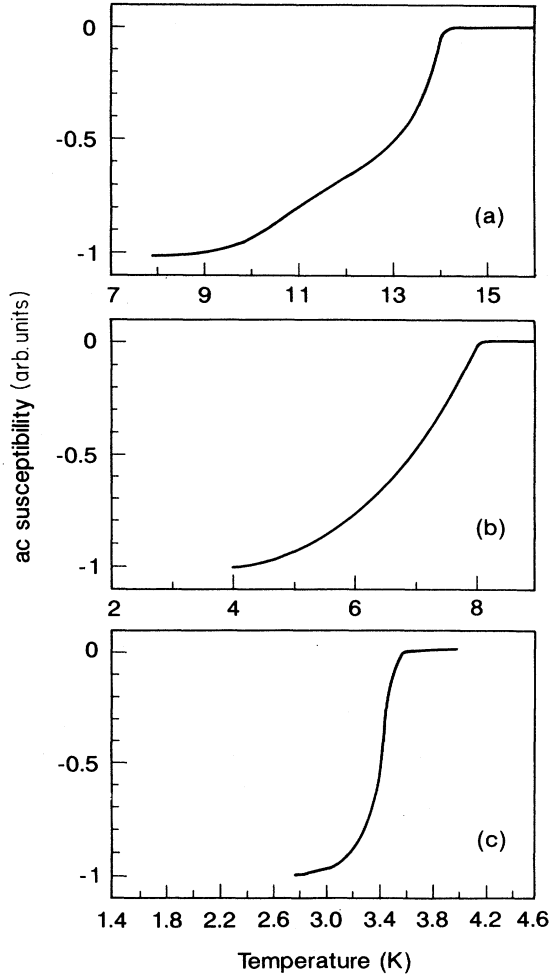


FIG. 2. Temperature dependence of ac susceptibility χ_{ac} in (a) SnMo_6S_8 , (b) $\text{SnMo}_6\text{S}_7\text{Se}$, and (c) $\text{SnMo}_6\text{S}_1\text{Se}_7$.

TABLE I. List of transition temperatures $T_{c,0}$, $T_{c,10\%}$, and $T_{c,\mu\text{SR}}$ of the samples investigated. Also listed are the $\sigma(0)$ following from the fit of Eq. (13) to $\sigma_G(T)$.

Sample	$T_{c,0}$ (K)	$T_{c,10\%}$ (K)	$T_{c,\mu\text{SR}}$ (K)	$\sigma(0)$ (μs^{-1})
$\text{SnMo}_6\text{S}_7\text{Se}_7$	3.6(1)	3.50(5)	4.3(2)	0.081(4)
$\text{SnMo}_6\text{S}_4\text{Se}_4$	5.25(10)	5.05(5)	4.7(1)	0.089(2)
$\text{SnMo}_6\text{S}_7\text{Se}_1$	8.1(1)	7.90(5)	7.02(3)	0.181(1)
SnMo_6S_8	14.0(1)	13.85(5)	13.81(1)	0.748(2)
$\text{PbMo}_6\text{S}_4\text{Se}_4$	4.45(10)	4.45(5)	4.5(3)	0.060(5)
PbMo_6S_8	14.7(1)	14.55(5)	14.41(1)	0.725(2)

For comparison with μSR data the magnetization was also measured during a field-cooling scan in an applied field of 0.3 T. The results are shown in Fig. 5.

B. Data acquisition

The transverse field μSR measurements were performed on the surface muon beam line $\pi\text{M}3$ of the proton accelerator at the Paul Scherrer Institute in Villigen, Switzerland, using a standard μSR spectrometer equipped with a He-flow cryostat.²⁶ This spectrometer allows the application of fields up to 0.3 T parallel to the momentum of the incoming μ^+ . A spin rotator in the beam line turns the μ^+ polarization from parallel to approximately perpendicular to the beam line, thus facilitating the observation of the μ^+ Larmor precession. Positrons from the μ^+ decay were recorded in four telescopes placed in a plane perpendicular to the field and the incoming μ^+ momentum. As usual the positron rate was measured and histogrammed as a function of elapsed μ^+ lifetime. The rate can be represented by the expression¹⁷

$$\begin{aligned} \frac{dN_{\mu^+}}{dt} &= N_0 e^{-t/\tau_\mu} \{1 + A_0 \mathbf{P}(t) \cdot \mathbf{r}_0\} + BG \\ &= N_0 e^{-t/\tau_\mu} \{1 + A_G(t) \cos(\omega_0 t + \phi)\} + BG, \end{aligned} \quad (10)$$

where \mathbf{r}_0 is a unit vector pointing along the axis of one of the positron telescopes, ϕ is a phase given by the angle between $\mathbf{P}(0)$ and \mathbf{r}_0 , τ_μ is the average μ^+ lifetime (2.2 μs), and BG is a time-independent background due to accidental decay events. $G(t)$ follows from Eq. (4) whereby it is understood that $F(\omega)$ is now representing the effective spectral distribution including all possible contributions as discussed in Sec. II.

The sample disks were oriented perpendicularly to the incoming μ^+ momentum and the magnetic field. The demagnetization factor $N_s/4\pi$ for the disc in this orientation was estimated to amount to 0.75, using tabulated values for cylinders given in Ref. 27. The incoming μ^+ beam was collimated so well that practically all μ^+ stopped in the sample and no background signal from the sample holder and/or cryostat walls could be detected.

All measurements were performed in the field-cooling mode, i.e., the external field was set at a temperature above T_c and the temperature was then lowered through T_c down to the base temperature of about 2.2 K. The external field was generally set to 0.3 T, but a few measurements were also performed in smaller fields.

TABLE II. List of “best” λ and σ_a values from a comparison of simulated and measured data. σ_{vortex} is calculated from λ with Eq. (7). T_{meas} is the temperature at which the analyzed spectra were measured. \bar{T}_c is an average transition temperature from Table I. * = σ_n .

Compound	T_{meas} (K)	\bar{T}_c (K)	λ (Å)	σ_{vortex} (μs^{-1})	σ_a (μs^{-1})
SnMo ₆ S ₁ Se ₇	2.25	3.8	10 900(600)	0.090	0.03*
SnMo ₆ S ₄ Se ₄	2.3	5.0	10 400(500)	0.100	0.03*
SnMo ₆ S ₇ Se ₁	2.4	7.6	6 500(600)	0.254	0.1
SnMo ₆ S ₈	5	13.9	2 400(250)	1.862	0.40(10)
PbMo ₆ S ₄ Se ₄	2.32	4.5	12 300(600)	0.071	0.03*
PbMo ₆ S ₈	3.0	14.5	2 400(250)	1.862	0.40(10)

As an example Fig. 3(a) shows the Fourier transform (real amplitude) obtained from a μSR signal taken in SnMo₆S₈ at 5 K and 0.3 T. Its shape reflects quite well the original shape of $F(\omega)$ in the mixed state of a type-II superconductor. It has a maximum (logarithmic singularity) at the saddle-point field h_s and a long tail to higher frequencies which ends at the maximum field h_{max} associated with the center of a vortex. The tail on the low-frequency side is much shorter and ends at the minimum field h_{min} , associated with the midpoint between a triangle of vortices.

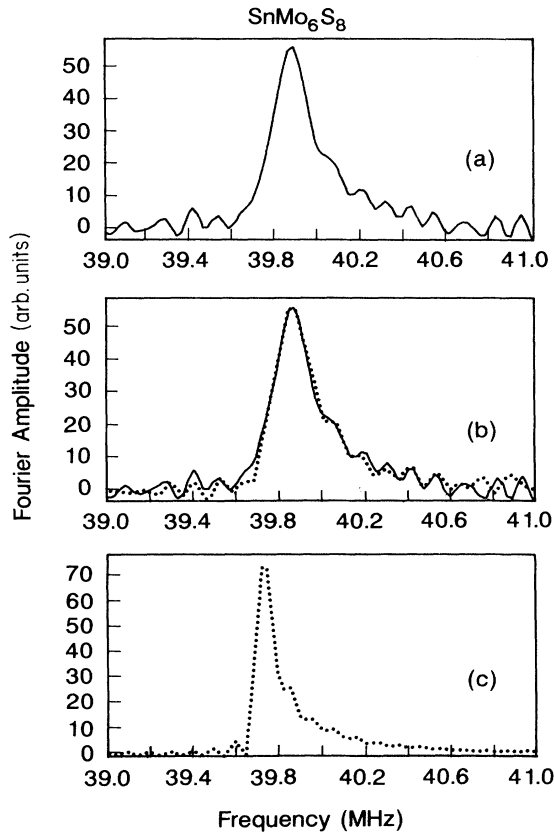


FIG. 3. Fourier transforms of measured and simulated μSR spectra: (a) from data taken at 5 K after field cooling in a field of 3 kG in SnMo₆S₈; (b) from simulated data generated with $\lambda=2400$ Å and $\sigma_a=0.4$ μs^{-1} (dotted curve) superimposed on the same experimental data as in (a); (c) from simulated data generated with $\lambda=2400$ Å and $\sigma_a=0$. Note the perfect agreement in shape and amplitude of the two curves in (b).

IV. RESULTS

A. Temperature scans

Simple Gaussian fits served to monitor the general trends of the average frequency ω_0 , the effective relaxation rate σ_G , and the signal amplitude A_0 as the temperature is lowered through T_c . Figure 4 displays results obtained for the sample SnMo₆S₈ at 0.3 T. As can be seen

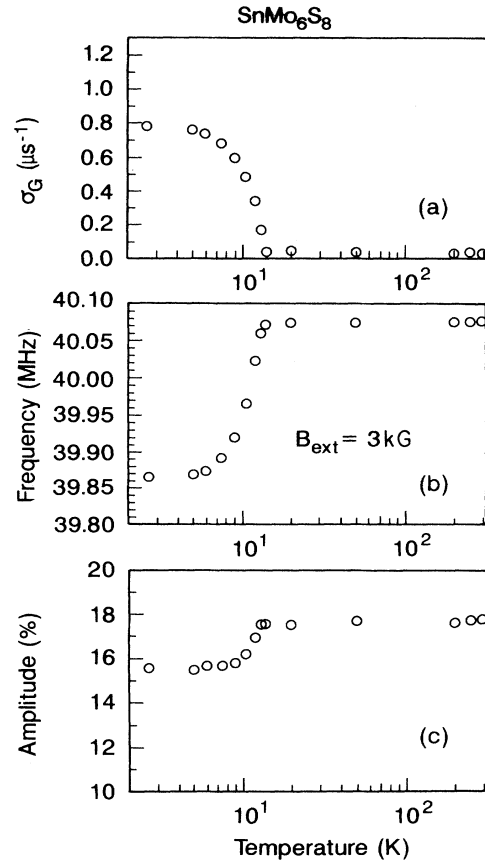


FIG. 4. Temperature dependence of (a) σ_G , (b) precession frequency ν_μ , and (c) signal amplitude A_0 in SnMo₆S₈ obtained from a field-cooling scan in $B_{\text{ext}}=3$ kG. The parameters result from fits of Eq. (10) to the μSR spectra assuming $G(t)$ to be given by Eq. (6). This assumption is strictly valid above T_c and breaks down below T_c as can be seen from the apparent decrease of A_0 (A_0 is an instrumental parameter independent of temperature).

all three parameters change abruptly when the temperature is lowered below T_c . The decrease of A_0 is an artifact of the fit and reflects the fact that a Gaussian function does not properly account for the true relaxation function $G(t)$ in the mixed state.

The decrease of the frequency below T_c reflects the diamagnetism of the sample in the superconducting state. According to Eq. (8) the average ω_0 is given by

$$\begin{aligned}\omega_0 &= \gamma_\mu \langle B_0 \rangle_{\text{grains}} \\ &= \gamma_\mu \left[B_{\text{ext}} + \left(\frac{4\pi}{3} - N_s \right) M_s + \frac{8\pi}{3} M_m \right] \\ &= \gamma_\mu \left\{ B_{\text{ext}} + \left[\left(\frac{4\pi}{3} - N_s \right) + \frac{8\pi}{3} \left(\rho_g / \rho_s \right) \right] \cdot M_s \right\},\end{aligned}\quad (11)$$

Indeed a perfect scaling of $\Delta\omega = \omega_0 - \gamma_\mu H_{\text{ext}}$ with the independently measured M_s (Ref. 25) is obtained as can be seen in Fig. 5. From this figure follows that $(4\pi/3 - N_s) + (8\pi/3)\rho_g/\rho_s \cong 2.89$. With $\rho_g/\rho_s = 1.25 - 1.33$, one then calculates $N_s \cong 4\pi/3$, which is incompatible with the shape of the sample. Alternatively using $N_s = 0.75 \times 4\pi$ one obtains $\rho_g \cong \rho_s$ which again is impossible. However, $\rho_g = \rho_s$ implies that $B_0 = B_{\text{ext}} + (4\pi - N_s)M_s$, which can be understood if the magnetization is primarily arising from intergrain currents in agreement with previous investigations on intra- and intergrain critical currents.²⁴ In other words the magnetization of individual grains can be neglected.

Above T_c one observes a generally very small and temperature independent relaxation rate of $\sigma_G = \sigma_n \cong (0.03 - 0.04) \mu\text{s}^{-1}$. The relaxation arises from the nuclear dipole fields originating mainly from the two Mo isotopes ^{95}Mo (abundance 16%) and ^{97}Mo (abundance 9.5%) and in the Pb compounds from ^{207}Pb (abundance 22%). The measured relaxation rates are consistent with the μ^+ being at a site at the center of the Mo_6X_8 cluster. However, other sites cannot be excluded.

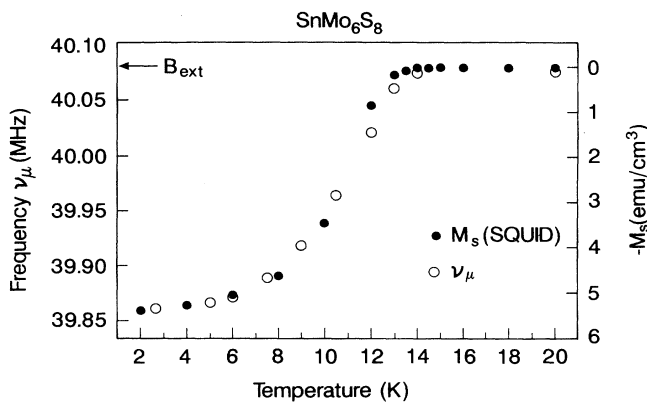


FIG. 5. Comparison of temperature dependence of ν_μ and magnetization M_s in SnMo_6S_8 . M_s was measured with a SQUID magnetometer by the same procedure as ν_μ (field-cooling scan in $B_{\text{ext}} = 3$ kG). Perfect scaling of ν_μ with M_s is observed. The M_s data were provided by Schilling (Ref. 25).

The increase of the relaxation rate σ_G below T_c reflects the formation of the flux-line lattice and mirrors the increasing internal field spread associated with it. To a certain extent (see Fig. 1), σ_G will be proportional to the “rms” width of $F(\omega)$, i.e., $\sigma_G \propto \sigma$ [Eq. (7)] $\propto 1/\lambda^2$. The increase of σ_G below T_c , therefore, arises from the temperature dependence of λ . Since it is not the purpose of this paper to study the temperature dependence of λ we will not discuss these data in more detail except to mention that they were used to obtain an independent determination of T_c from the onset of the rise of $\sigma_G(T)$. To this end we assumed that $\lambda(T)$ follows the usual two-fluid model formula, e.g.,

$$\lambda(T) = \lambda(0) / \sqrt{1 - (T/T_c)^4}, \quad (12)$$

and we fitted the relaxation rates $\sigma_G(T)$ with the formula

$$\sigma_G^2(T) - \sigma_n^2 = \sigma^2(0) [1 - (T/T_c)^4]^2 \quad (13)$$

restricted to the interval where $\sigma(T) > \sigma_n$. The results on $T_c (= T_{c,\mu\text{SR}})$ and $\sigma(0)$ are listed in Table I. Two fits for compounds with rather different T_c are displayed in Figs. 6 and 7.

B. Determination of $\lambda(0)$

$\lambda(0)$ was extracted from the lowest temperature runs following the procedure described in detail in Ref. 20. This procedure consists of a comparison of simulated and measured data. One starts from the London equations, assuming a certain λ and calculates the resulting $F(\omega)$. In a second step $F(\omega)$ is convoluted with a Gaussian distribution with a certain width σ_a . Then an artificial μSR spectrum (histogram) dN_e^+/dt is generated from the convoluted frequency distribution, taking into account also the μ^+ decay and superimposing Gaussian noise, which now looks like Eq. (10). The spectrum is restricted to the time range of the measured histograms (8.5 μs). Hence the analysis of the simulated data involves the same limited time range as in the experiment. The simulated μSR spectra can now be Fourier transformed or can be analyzed by direct fits of Eq. (10) with $G(t)$ given by Eq. (6). Also so-called two-component fits were carried out, in

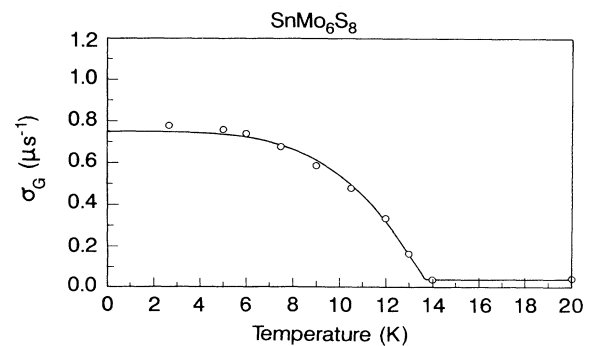


FIG. 6. Temperature dependence of σ_G in SnMo_6S_8 from a field-cooling scan at 3 kG [same as in Fig. 4(a)]. The solid line represents a fit of Eq. (13) to the data with $\sigma_n = 0.035(1) \mu\text{s}^{-1}$.

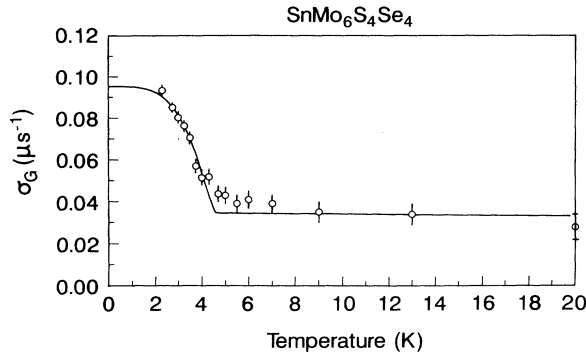


FIG. 7. Temperature dependence of σ_G in $\text{SnMo}_6\text{S}_4\text{Se}_4$ from field-cooling scan at 3 kG. The solid line is a fit of Eq. (13) to the data with $\sigma_n = 0.034(2) \mu\text{s}^{-1}$.

which Eq. (4) is approximated by

$$P_x(t) = A_1 \exp(-\frac{1}{2}\sigma_1^2 t^2) \cos\omega_1 t + A_2 \exp(-\frac{1}{2}\sigma_2^2 t^2) \cos\omega_2 t. \quad (14)$$

This formula can account to a certain extent for the asymmetric distribution of $F(\omega)$. Experimental data are analyzed in the same threefold way. The input parameters λ and σ_a are now varied until simulated and measured spectra coincide within their statistical noise. A particularly sensitive quantity is the maximum amplitude of the Fourier transform, while its shape is less sensitive and could be very similar for different λ , σ_a pairs. Good agreement was claimed when Fourier-transform amplitudes and the parameters from one- and two-component fits agreed within their error bars. As an example Fig. 3 shows (a) the real amplitude of the Fourier transform from data taken at 5 K and 0.3 T in the SnMo_6S_8 sample, (b) the same Fourier transform and the “best” Fourier transform from simulated data with the input values $\lambda = 2400 \text{ \AA}$ and $\sigma_a = 0.4 \mu\text{s}^{-1}$, and (c) a simulated Fourier transform with $\lambda = 2400 \text{ \AA}$ but $\sigma_a = 0$. Another example is shown in Fig. 8 for the compound $\text{SnMo}_6\text{S}_7\text{Se}$. Fourier spectra from the compounds $\text{SnMo}_6\text{S}_4\text{Se}_4$, $\text{SnMo}_6\text{S}_1\text{Se}_7$, and $\text{PbMo}_6\text{S}_4\text{Se}_4$ did not show any visible broadening exceeding the width given by the minimum resolution of the fast Fourier-transform routine. In this

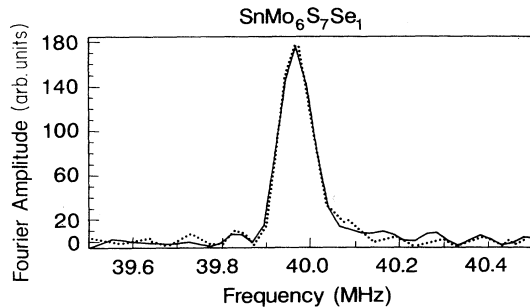


FIG. 8. Fourier transforms from a measured μSR spectrum ($\text{SnMo}_6\text{S}_7\text{Se}_1$) after field cooling to 2.4 K and from a simulated spectrum with $\lambda = 6500 \text{ \AA}$ and $\sigma_a = 0.1 \mu\text{s}^{-1}$. Note again the perfect agreement.

case only one- and two-component fits were used in the determination of λ . Table II lists the results obtained from the above analysis together with σ_{vortex} calculated from Eq. (7). The results are also indicated in Fig. 1 by crosses, where σ_G was determined from Gaussian one-component fits. It is seen that σ_{vortex} deviates considerably from $\sigma(0)$ in Table I for compounds with the smallest λ .

The additional broadening of $0.4 \mu\text{s}^{-1}$ for the $(\text{Pb},\text{Sn})\text{Mo}_6\text{S}_8$ samples is smaller than what could be expected on the basis of Eq. (9). Neglecting the distribution in demagnetization factors (i.e., $\Delta N_g = 0$) $\sigma_a = 0.4 \mu\text{s}^{-1}$ implies a width $\Delta B \simeq 4.7 \text{ G} \simeq 4\pi(0.07 M_s)$, which points to rather small ($\sim 1\%$) random displacement of the vortices. $\Delta N_g = 0$ is consistent with the observation that M_s arises mainly from intergrain currents and that the intragrain magnetization seems to be rather unimportant.²⁴

C. Field dependence of $\sigma(0)$

In $\text{SnMo}_6\text{S}_4\text{Se}_4$ and SnMo_6S_8 field-cooling temperature scans were also carried out at fields smaller than 3 kG. Results on $\sigma(0)$ are displayed in Figs. 9(a) and 10. A very strong dependence is observed for fields below $\sim 500 \text{ G}$ in $\text{SnMo}_6\text{S}_4\text{Se}_4$ and below 2 kG in SnMo_6S_8 . Interestingly the increase in the relaxation rate is accompanied by a decrease in the sample magnetization $|M_s(T=0)|$ extracted from the frequency shift $\Delta\omega(T=0)$ [see Fig. 9(b)]. We interpret this as evidence for strong pinning at moderate fields, where the pinning interactions can be ex-

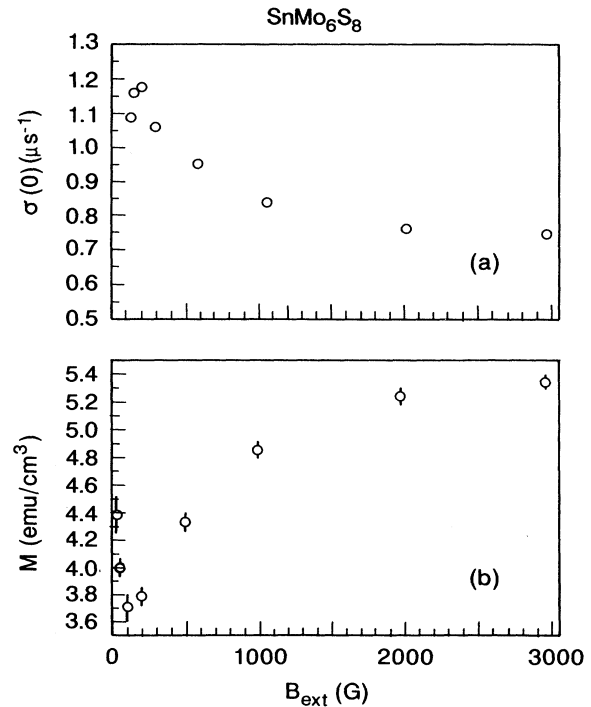


FIG. 9. Field dependence of (a) $\sigma(0)$ and (b) magnetization M_s in SnMo_6S_8 . M_s was determined from the frequency shift $\nu_\mu - \gamma/2\pi \times B_{\text{ext}}$ using Eq. (11) and assuming $N_s = 0.77 \times 4\pi$ and $\rho_g = \rho_s$.

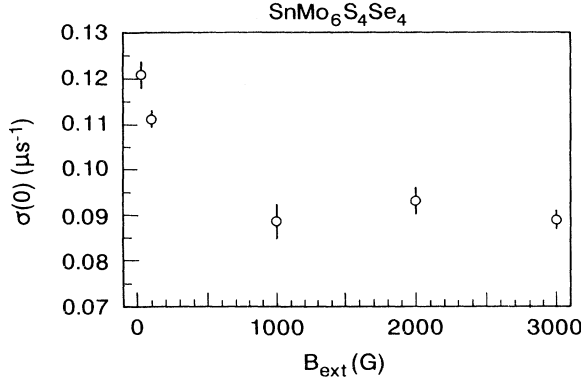


FIG. 10. Field dependence of $\sigma(0)$ in $\text{SnMo}_6\text{S}_4\text{Se}_4$.

pected to prevail over the intervortex interaction, due to the increased distance between vortices. For higher vortex densities the intervortex interaction will become dominant and flux expulsion (leading to the diamagnetism) will be more effective. The decrease of $\sigma(0)$ and the concomitant rise in $|M_s|$ at very low fields is not understood at present. It does not seem to be related to H_{c1} , since, due to the demagnetization field, the effective H_{c1} is much smaller [$H_{c1,\text{eff}} = (1 - N_s/4\pi)H_{c1}$].

The data indicate, however, that at $H_{\text{ext}} = 3 \text{ kG}$ a rather regular flux-line lattice is established for which the internal field distribution width is independent of the flux-line density.

V. DISCUSSION

A. Penetration depth in SnMo_6S_8 and PbMo_6S_8

The actual penetration depth is not only a function of n_s [Eq. (1)], but, depending on the sample purity and homogeneity, also a function of the electron mean free path l [Eq. (2)]. The mean free path l can be estimated from resistivity measurements. Assuming that at room temperature l is limited by the rhombohedral lattice spacing $a_R = 6.5 \text{ \AA}$, l at low temperatures is estimated to be²⁸

$$l(T \rightarrow 0\text{K}) > \frac{\rho(RT)}{\rho(T_c + \epsilon)} 6.5 \text{ \AA} . \quad (15)$$

For SnMo_6S_8 and PbMo_6S_8 , $\rho(RT)/\rho(T_c + \epsilon)$ is measured to amount to typically ~ 6 – 12 and hence $l(0) \cong 40$ – 60 \AA .²⁸ However, since our estimate of the resistivity includes the intergrain contribution, we believe that the real intragrain mean free path is larger than this estimation. The Landau-Ginsberg coherence length ξ can be obtained from the relation¹⁶

$$H_{c2} = \frac{\Phi_0}{2\pi\xi^2} . \quad (16)$$

With $H_{c2} = 30 \text{ T}$ for SnMo_6S_8 and 60 T for PbMo_6S_8 one gets $24 \text{ \AA} < \xi < 34 \text{ \AA}$, which lead to $\xi/l < 0.5$. This shows that these samples are in between the clean and dirty limit. Therefore the London penetration depth λ_L for both samples is ranging from 2400 \AA in the clean lim-

it down to 2000 \AA if we correct the experimental value of λ listed in Table II with Eq. (2). On the other hand, with samples having substitutions on the chalcogen sites the dirty limit is more appropriate, since these types of substitutions strongly decrease the mean free path.

Our λ value (Table II) can be used to calculate H_{c1} from¹⁶

$$H_{c1} = \frac{\phi_0}{4\pi\lambda^2} \ln \left[\frac{\lambda}{\xi} \right] = 130(25) \text{ gauss} , \quad (17)$$

in good agreement with the value measured by SQUID on the SnMo_6S_8 sample (see Sec. III A).

Less consistency is observed when correlating our data with the thermodynamic critical field $H_c(0)$, which in PbMo_6S_8 is found to be 2.195 kG .³⁰ Using the expression¹⁶

$$H_c = \frac{1}{2\pi\sqrt{2}} \frac{\phi_0}{\lambda\xi} \quad (18)$$

and $\xi = 24 \text{ \AA}$, one predicts $\lambda = 3300 \text{ \AA}$; or with $\lambda = 2400 \text{ \AA}$, $\xi = 33.3 \text{ \AA}$.

In order to determine n_s and m^* independently from λ_L we need more information, which can be obtained from the electronic specific heat (Sommerfeld constant)

$$\gamma = \frac{k_B^2 m^*}{\hbar^2} \left[\frac{\pi^2 n_s}{9} \right]^{1/3} , \quad (19)$$

assuming that γ can be approximated by the free-electron gas formula. It is hereby assumed that the density of superconducting carriers agrees with the normal-state carrier density. γ of our SnMo_6S_8 sample has been measured by Cors²⁹ yielding $\gamma_{\text{Sn}} = 76.4(1.5) \text{ mJ/K}^2 \text{ mol}$. Cors³⁰ has also measured γ of a PbMo_6S_8 sample which had been prepared in a similar way as the present one yielding $\gamma_{\text{Pb}} = 97.5 \text{ mJ/K}^2 \text{ mol}$. Combining Eq. (1) and Eq. (19) we arrive at

$$n_s = 8.7(1.3) \times 10^{21} \text{ cm}^{-3} ,$$

$$m^*/m_0 = 14(4) \text{ for } \text{SnMo}_6\text{S}_8$$

and

$$n_s \cong 10.5 \times 10^{21} \text{ cm}^{-3}; m^*/m_0 \cong 16 \text{ for } \text{PbMo}_6\text{S}_8 .$$

The errors on the latter values are at least as large as for SnMo_6S_8 .

These results are in reasonable agreement with $n_s = 6 \times 10^{21} \text{ cm}^{-3}$ and $m^*/m = 8.2$ obtained from magneto-optical studies on PbMo_6S_8 by Fumagalli and Schoenes.³¹ Also Hall-effect measurements in EuMo_6S_8 , SrMo_6S_8 , and the series $\text{Eu}_x\text{Sn}_{1-x}\text{Mo}_6\text{S}_8$ ($x = 0.6, 0.8, 0.9$) at room temperature have led to Hall coefficients varying between $R_H \cong +0.5 \times 10^{-3} \text{ cm}^3/\text{G}$ and $R_H = +0.9 \times 10^{-3} \text{ cm}^3/\text{G}$ implying effective carrier concentrations of $n_{\text{eff}} = (7 \times 10^{21} - 1.24 \times 10^{22}) \text{ cm}^{-3}$.¹⁵

This order of magnitude has to be contrasted with predictions based on electronic structure considerations which yield an equal number of hole and electron charge carriers with $n = n_{\text{hole}} = n_{\text{electron}} \cong 1 \times 10^{21} \text{ cm}^{-3}$.¹⁵ Based

on these numbers the Hall coefficient was explained to reflect primarily the hole and electron mobilities. The positive sign of R_H indicates in any case that conduction by holes prevails over conduction by electrons. The close agreement of n_s extracted from λ_L and from Ref. 31 with the effective charge-carrier concentration extracted from R_H could indicate that only holes are involved in both the room-temperature transport and the low-temperature superconductivity. Taking 280 \AA^3 for the volume of the rhombohedral unit cell, the number of hole carriers per unit cell is of the order of 2.8.

B. Correlation of T_c and n_s

A straightforward extraction of n_s from λ of the Se-doped samples is hampered by a lack of information on the electron mean free path l , the coherence length ξ_0 , and the Sommerfeld constant γ . l is expected to decrease with increasing Se content (at least up to $x=4$) and ξ_0 may increase, as can be inferred from the decline of H_{c2} in the series $\text{PbMo}_6\text{S}_{8-x}\text{Se}_x$ ($x \leq 2.5$).³² The increase of λ in the Se-doped samples may just reflect then the trend in ξ_0/l . In the worst case l could be as small as $a_R = 6.5 \text{ \AA}$, which would imply $\xi_0/l \gtrsim 2$ and hence $\lambda/\lambda_L \gtrsim \sqrt{3}$. This could certainly account, at least in part, for the increase of λ . On the other hand, in the dirty limit, H_{c2} can be approximated by¹

$$H_{c2} \sim \frac{1}{lv_F} T_c, \quad (20)$$

where v_F is the Fermi velocity. According to Ref. 32, H_{c2} scales reasonably well with T_c which could imply that l is rather independent of the Se content provided v_F is independent of x , too. On the basis of this latter argument we will assume that the increase of λ across the series $\text{MMo}_6\text{S}_{8-x}\text{Se}_x$ reflects mainly the behavior of λ_L , i.e., it reflects the x dependence of n_s/m^* .

Figures 11 and 12 correlate T_c and $\sigma_{\text{vortex}} \propto 1/\lambda^2 \propto n_s/m^*$ in two different ways. Included in these plots are two data points (LaMo₆Se₈, PbMo₆S₈) tak-

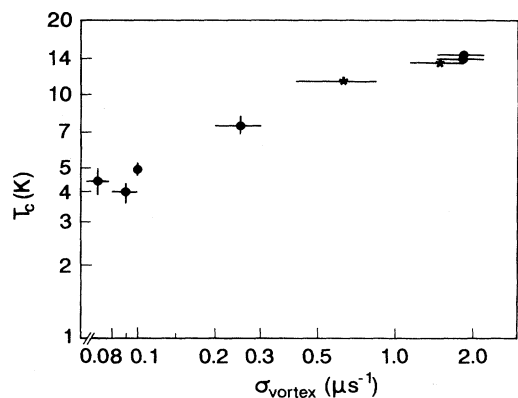


FIG. 11. Log-log plot of T_c versus σ_{vortex} [Eq. (7)]. T_c is identified with \bar{T}_c (Table II) and ΔT_c with half the scatter of the T_c values in Table I. Included are two data points from Ref. 6 (*).

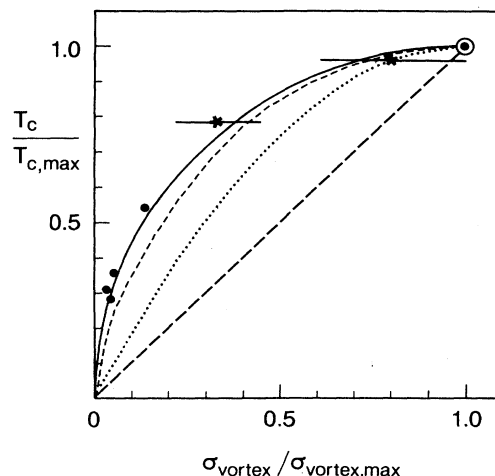


FIG. 12. Plot of $t = T_c/T_{c,\text{max}}$ versus $\rho = \sigma_{\text{vortex}}/\sigma_{\text{vortex,max}}$ (see text for $T_{c,\text{max}}$ and $\sigma_{\text{vortex,max}}$). The solid line is given by $t^2 + (1-s)^2 = 1$ [Eq. (21)], the dotted line by Eq. (24), and the short dashed line by Eq. (28) (with $\gamma=1$). The long dashed line represents the original conjecture of Uemura *et al.* ($T_c \propto n_s$) (Ref. 6).

en from Uemura *et al.*⁶ We used their σ_G values to estimate σ_{vortex} with the help of Fig. 1 by assuming that their data interpolate smoothly our data (crosses in Fig. 1). In Fig. 11, T_c of each sample is plotted versus the corresponding σ_{vortex} . The double logarithmic plot suggests a power-law dependence which comes close to $T_c \propto \sigma_{\text{vortex}}^{1/3}$, i.e., it seems to be quite different from the correlation of T_c and σ_G in the high-temperature superconductors, particularly in the 1-2-3 compounds. In Fig. 12, following Ref. 9, we plot $t = T_c/T_{c,\text{max}}$ versus $s = \sigma_{\text{vortex}}/\sigma_{\text{vortex,max}}$, assuming that $T_{c,\text{max}}$ and $\sigma_{\text{vortex,max}}$ are given by the results in the ‘‘homogeneous’’ samples PbMo_6S_8 ($\bar{T}_c = 14.5 \text{ K}$, $\sigma_{\text{vortex,max}} = 1.86 \mu\text{s}^{-1}$) and SnMo_6S_8 ($\bar{T}_c = 13.9 \text{ K}$, $\sigma_{\text{vortex,max}} = 1.86 \mu\text{s}^{-1}$). For LaMo_6Se_8 we assume $T_{c,\text{max}} \cong 14 \text{ K}$. Surprisingly the data points fall almost on a circular line, defined by

$$t^2 + (1-s)^2 = 1 \quad (21)$$

and hence

$$t = [s(2-s)]^{1/2} \quad (22)$$

or, with Eqs. (1) and (7),

$$t = \left[\frac{n_s}{n_{s,\text{max}}} \left[2 - \frac{n_s}{n_{s,\text{max}}} \right] \right]^{1/2}, \quad (23)$$

assuming that m^* is the same for all the present compounds. For $n_s/n_{s,\text{max}} \ll 1$, $t \propto \sqrt{n_s}$.

This empirical dependence can now be compared with several predictions. Schneider and Keller⁹ consider a three-dimensional (3D) extreme type-II superconductor with very short correlation length and treat the emergence of superconductivity in analogy to superfluidity in ⁴He (formation of local pairs). On the basis of this model T_c is predicted to follow the expression

$$t = n_s / n_{s,\max} (2 - n_s / n_{s,\max}) . \quad (24)$$

This expression is represented by the dotted curve in Fig. 12. It reproduces the data badly.

Using a quantum percolation model, Dallacasa and Feduzi³³ derive the expression

$$T_c \propto \varepsilon_F \left[1 - \frac{n_s}{n_{s,c}} \right]^\gamma , \quad (25)$$

where ε_F is the Fermi energy, $n_{s,c}$ denotes the percolation threshold and γ is a critical exponent. For a three-dimensional material $\varepsilon_F \propto n_s^{2/3}$. (In the more 2D high- T_c systems $\varepsilon_F \propto n_s$.) The maxima of $T_c, T_{c,\max}$ and of $n_s, n_{s,\max}$ is given by

$$T_{c,\max} = n_{s,\max}^{2/3} \left[1 - \frac{2}{2+3\gamma} \right]^\gamma \quad (26)$$

and

$$n_{s,\max} = \frac{2}{2+3\gamma} n_{s,c} . \quad (27)$$

Hence

$$t = \frac{T_c}{T_{c,\max}} = \left[2 - \frac{4}{2+3\gamma} \right]^{-\gamma} \left[\frac{n_s}{n_{s,\max}} \right]^{2/3} \times \left[2 - \frac{4}{2+3\gamma} \frac{n_s}{n_{s,\max}} \right]^\gamma . \quad (28)$$

The resulting curve for $\gamma=1$ is also displayed in Fig. 12. This curve (short dashed line) is quite close to the data. For quantum percolation in a 3D system a critical exponent of $\gamma=1$ is predicted ($\gamma=0.9$ in classical percolation). With $n_{s,\max} \approx 2.8$ carriers per unit cell the percolation threshold would be $n_{s,c} = 5/2 \times n_{s,\max} \approx 7$ carriers per unit cell or about one carrier per Mo atom. This is perhaps a reasonable value. It would be interesting to find an example where $\sigma_{\text{vortex}}/\sigma_{\text{vortex}}(T_{c,\max}) > 1$ and $T_c < T_{c,\max}$ to test also a regime closer to the percolation limit. Such a point is indeed quoted in Ref. 6 but the error involved in estimating σ_{vortex} from σ_G is so large that its inclusion in the present discussion is not justified.

Uemura and co-workers^{6,10} have argued that the low carrier density Chevrel-phase compounds follow their universal T_c versus n_s curve found for underdoped high-temperature superconductors. According to their model $T_c \propto \varepsilon_F \propto n_s^{2/3}/m^*$ for a 3D system. The present data, where T_c is correlated with the absolute values of $1/\lambda^2$, do certainly not comply with this prediction.

Despite all the uncertainties in trying to correlate T_c with n_s (m^*/m is assumed constant, ξ/l is assumed to be roughly independent of x and smaller than 1), the obtained simple empirical relationship is suggestive of a deeper meaning. By comparison with some theoretical models it appears as if a quantum percolation model describes the data most closely, involving moreover reasonable values for the critical exponent γ and the percolation threshold $n_{s,c}$. The particular crystal structure of

the ternary Chevrel-phase compounds, possessing relatively isolated Mo_6X_8 building blocks and nearly localized electronic states, may lend itself as a good candidate for a percolative behavior.

VI. SUMMARY

We have presented low-temperature results from a systematic study of the width of the internal field distribution after field cooling at 3 kG through T_c in the mixed state of several Chevrel-phase superconductors: $\text{PbMo}_6\text{S}_{8-x}\text{Se}_x$ ($x=0,4$), $\text{SnMo}_6\text{S}_{8-x}\text{Se}_x$ ($x=0,1,4,7$). In order to obtain absolute values of the penetration depth λ simulated data, generated for a certain λ , were compared with experimental results. The simulations included additional broadening contribution, assumed to be of Gaussian shape, which were convoluted with the spectral distribution associated with the flux-line lattice. Very good agreement could be obtained between measured and simulated data leading to an unambiguous determination of the penetration depth λ and an additional Gaussian width σ_a . The magnitude of σ_a is smaller than expected and points to the establishment of a rather regular flux-line lattice. Even if the residual distortion should not strictly be accountable for in terms of a Gaussian distribution, we do not think that the present Gaussian assumption will effect to any noticeable degree the extracted λ values. By combining the result $\lambda \approx 2400 \text{ \AA}$ with other known parameters (electron mean free path, Sommerfeld constant γ , H_{c2}) the density of superconducting carriers n_s and the effective mass m^* could be extracted separately with $n_s \approx 9 \times 10^{21} \text{ cm}^{-3}$ and $m^* \approx 15m_0$ for both SnMo_6S_8 and PbMo_6S_8 . The Ginsburg-Landau parameter is determined to be $\kappa=100(10)$. The carrier density of nearly 10^{22} cm^{-3} is consistent with magneto-optical measurements and with the effective density following from the room-temperature Hall coefficient. The latter is positive and thus points to holes as the charge carriers. The present value for the density is incompatible with estimates following from band-structure considerations. $\sigma_{\text{vortex}} \propto 1/\lambda^2$ shows an interesting correlation with the critical temperature T_c . Assuming a constant m^* and negligible effect of the carrier mean free path l , T_c shows a dependence on n_s which comes very close to a prediction based on a quantum percolation model.³³ A recently suggested universal T_c versus n_s curve, based on local pair formation in analogy to superfluid ^4He ,⁹ cannot accommodate the present results. Previous discussions on the nature of the dependence of T_c on the charge-carrier density (see introduction) have to be looked at from a new perspective. In particular the change of T_c is probably unrelated to the breakdown of the threefold rotational symmetry around the hexagonal c axis as the S atoms are substituted in part by Se atoms.

It is now of highest interest to extend the present studies to additional Chevrel-phase superconductors, on the one hand to pin down the n_s dependence of T_c more

firmly and on the other hand to find out whether there is a range where T_c will decrease, while n_s still increases.

Finally, we mention that attempts to measure the penetration depth also in the compound $\text{Eu}_{0.75}\text{Sn}_{0.25}\text{Mo}_6\text{S}_{7.6}\text{Se}_{0.4}$, which shows field-induced superconductivity in a second field range above H_{c2} (Jaccarino-Peter effect),³⁴ failed due to the strong magnetism of the Eu^{2+} ions, which lead to a very rapid depolarization of the transverse field μSR signal.³⁵

ACKNOWLEDGMENTS

We thank D. Herlach (now at PSI) for allowing us to use the μSR spectrometer of the Stuttgart group, A. Schilling (ETH Zürich) for performing the SQUID measurements, and M. Affronte, Y. Jeanrenaud, S. Ritter, and A. Stettler (Genève) for technical support in the sample preparations and the χ_{ac} and x-ray measurements. We thank Professor H. R. Ott for his continuous encouragement and interest in this work.

*Present address: Meson Science Laboratory, University of Tokyo, Tokyo, Japan.

†Present address: Department of Physics, Rice University, Houston, TX 77251.

¹Ø. Fischer, *Appl. Phys.* **16**, 1 (1978).

²Y. J. Uemura, V. Z. Emery, A. R. Moodenbaugh, M. Suenaga, D. C. Johnston, A. J. Jacobson, J. T. Lewandowski, J. H. Brewer, R. F. Kiefl, S. R. Kretzman, G. M. Luke, T. M. Rieseman, C. E. Stronach, W. J. Kossler, J. R. Krempton, X. H. Yu, D. Opie, and H. E. Schone, *Phys. Rev. B* **38**, 909 (1988).

³B. Pümpin, H. Keller, W. Kündig, I. M. Savić, J. W. Schneider, H. Simmler, P. Zimmermann, E. Kaldis, S. Rusiecki, and C. Rossel, *Hyperfine Interact.* **63**, 25 (1990).

⁴E. J. Ansaldo, Ch. Niedermayer, J. L. Tallon, D. M. Pooke, J. H. Brewer, G. D. Morris, and S. R. Kretzmann, *Phys. Lett. A* **158**, 479 (1991).

⁵C. Parracchini, L. Romanó, and S. Bellini, *Physica C* **192**, 443 (1992).

⁶Y. J. Uemura, L. P. Le, G. M. Luke, B. J. Sternlieb, W. D. Wu, J. H. Brewer, T. M. Rieseman, C. L. Seaman, M. B. Maple, M. Ishikawa, D. G. Hinks, J. D. Jorgensen, G. Saito, and H. Yamochi, *Phys. Rev. Lett.* **66**, 2665 (1991).

⁷R. Friedberg, T. D. Lee, and H. C. Ren, *Phys. Lett. A* **152**, 417 (1991); **152**, 423 (1991).

⁸T. Schneider, *Z. Phys. B* **88**, 249 (1992).

⁹T. Schneider and H. Keller, *Phys. Rev. Lett.* **69**, 3374 (1992).

¹⁰Y. J. Uemura, A. Keren, L. P. Le, G. M. Luke, B. J. Sternlieb, W. D. Wu, J. H. Brewer, R. L. Whetten, S. M. Huang, Sophia Lin, R. B. Kaner, F. Diederich, S. Donovan, G. Grüner, and K. Halczer, *Nature (London)* **352**, 605 (1992).

¹¹M. Sergent, R. Chevrel, C. Rossel, and Ø. Fischer, *J. Less-Common Met.* **58**, 179 (1978).

¹²K. Yvon and A. Paoli, *Solid State Commun.* **24**, 41 (1977).

¹³R. Chevrel, M. Sergent, and Ø. Fischer, *Mater. Res. Bull.* **10**, 1169 (1975).

¹⁴M. Sergent, Ø. Fischer, M. Decroux, C. Perrin, and R. Chevrel, *J. Solid State Chem.* **22**, 87 (1977).

¹⁵H. W. Meul, *Helv. Phys. Acta* **59**, 417 (1986).

¹⁶See, e.g., D. Saint-James, G. Sarma, and E. J. Thomas, *Type-II Superconductivity* (Pergamon, Oxford, 1969).

¹⁷A. Schenck, *Muon Spin Rotation Spectroscopy* (Hilger, Bristol, 1985).

¹⁸P. Birrer, Doctoral thesis, ETH Zürich, 1991; P. Birrer, D. Cattani, J. Cors, M. Decroux, Ø. Fischer, F. N. Gygax, B. Hitti, E. Lippelt, A. Schenck, and M. Weber, *Hyperfine Interact.* **63**, 103 (1990).

¹⁹E. H. Brandt, *Phys. Rev. B* **37**, 2349 (1988).

²⁰M. Weber, A. Amato, F. N. Gygax, A. Schenck, H. Maletta, V. N. Duginov, V. G. Grebinnik, A. B. Lazarev, V. G. Olshevsky, V. Yu. Pomjakushin, S. N. Shilov, V. A. Zhukov, B. F. Kirillov, A. V. Pirogov, A. N. Ponomarev, V. G. Storchak, S. Kapusta, and J. Bock, *Phys. Rev. B* **48**, 13 022 (1993).

²¹E. H. Brandt, *J. Low Temp. Phys.* **73**, 355 (1988).

²²P. Birrer, F. N. Gygax, B. Hettich, B. Hitti, E. Lippelt, H. Maletta, A. Schenck, and M. Weber, *Physica C* **158**, 230 (1989).

²³M. Decroux *et al.*, *Proceedings of the International Workshop on Chevrel-Phase Superconductors*, edited by Ø. Fischer (University of Geneva, Geneva, 1991), p. 19.

²⁴D. Cattani, Ph.D. thesis, University of Geneva, 1990. D. Cattani, J. Cors, M. Decroux, and Ø. Fischer, *IEEE Trans. Magn. MAG-27*, 950 (1991).

²⁵A. Schilling (private communication).

²⁶W. Schwarz, diploma thesis, University of Heidelberg, 1987.

²⁷W. Kirenski, *Magnetismus* (Teubner, Leipzig, 1969).

²⁸R. Flückiger, R. Baillif, and E. Walker, *Mater. Res. Bull.* **13**, 743 (1978).

²⁹J. Cors (private communication).

³⁰J. Cors, Ph.D. thesis, University of Geneva, 1990.

³¹P. Fumagalli and P. Schoenes, *Phys. Rev. B* **44**, 2246 (1991).

³²M. Decroux, Ph.D. thesis, University of Geneva, 1987.

³³V. Dallacasa and R. Feduzi, *Phys. Lett. A* **170**, 153 (1992).

³⁴H. W. Meul, C. Rossel, M. Decroux, Ø. Fischer, G. Remenyi, and A. Briggs, *Phys. Rev. Lett.* **53**, 497 (1984).

³⁵P. Birrer, F. N. Gygax, B. Hitti, E. Lippelt, A. Schenck, D. Cattani, J. Cors, M. Decroux, Ø. Fischer, and S. Barth, *Hyperfine Interact.* **50**, 503 (1989).